Catalysis Today 153 (2010) 111–117

Contents lists available at ScienceDirect

Catalysis Today

journal homepage: www.elsevier.com/locate/cattod

# Influence of $H_2/O_2$ redox treatments at different temperatures on Pd-$CeO_2$ catalyst: Structure and oxygen storage capacity

Bin Wang, Duan Weng*, Xiaodong Wu, Jun Fan

*State Key Laboratory of New Ceramics & Fine Process, Department of Materials Science and Engineering, Tsinghua University, Beijing 100084, China*

ARTICLE INFO

*Article history:*
Available online 23 March 2010

*Keywords:*
Palladium
Ceria
Redox treatment
Oxygen storage capacity
Structure reorgnaization

ABSTRACT

In order to investigate the metal–support interaction in PM-$CeO_2$ system, a Pd-doped $CeO_2$ catalyst was prepared by the sol–gel method and was treated in the $H_2$–$O_2$ redox atmosphere at 300, 500 and 800 °C, respectively. The Brunauer–Emmett–Teller (BET), X-ray diffraction (XRD) and temperature-programmed reduction (TPR) results indicate that the redox treatment at 300 °C mainly affect the surface properties of the catalyst, while those at higher temperatures have an influence on the bulk properties. The step-scanning XRD and Raman results prove that Pd species on the surface of the sample mainly exist in the form of bulk Pd and PdO crystallites after the redox treatment at 500 °C, which are encapsulated by $CeO_2$ particles after the treatment at 800 °C. The CO oxidation activity, dynamic oxygen storage capacity (DOSC) and oxygen storage complete capacity (OSCC) of the catalyst vary with the treating temperature. The 300 °C-treated sample presents the highest activity for CO oxidation and oxygen storage capacity. The reduction-ratio dependent activation energy ($E_a$) is extremely low for the surface reduction of this sample, suggesting the participation of highly active oxygen. The active oxygen are suggested to originate from the enlarged Pd-Ce interface, which depends on the avaibility of surface Pd sites and contact between metal and support.



## 1. Introduction

In recent years, $CeO_2$-supported noble metal catalysts have attracted much attention due to their application in automotive exhausts purification and other industrial applications [1–2]. Generally, precious metals (PM) are impregnated on ceria or ceria–zirconia with alumina as carrier in three-way catalysts (TWCs) [3–5]. Some researches indicated that in conventional catalysts, only the surface atoms of the noble metal particles serve as adsorption sites, and even in 4–6 nm metal particles, only 1/4 to 1/5 of the total noble metal atoms are utilized for catalytic conversion [6]. Hedge' group developed a solution combustion method for synthesizing dispersed noble metal ionic catalysts [7–10], as well as did by the Medina and co-workers [11]. When precious metals are doped into the ceria or titania lattice, the higher activity for CO, $NO_x$ and hydrocarbons conversions can be achieved in comparison with the supported catalysts with the same PM addition. The possible reasons for this improvement include full utilization of precious metals, activation of lattice oxygen in the support oxide and high oxygen storage capacity caused by the effect of PM insertion. In our former work, a $Ce_{0.66}Zr_{0.32}Pt_{0.02}O_2$ catalyst was synthesized by sol–gel method and Pt was confirmed to be inserted into the ceria lattice by XRD, XPS and TPR analyses [12]. The insertion of platinum brought about a different synergistic effect between Pt and Ce in $Ce_{0.66}Zr_{0.32}Pt_{0.02}O_2$ compared with the $Pt/Ce_{0.67}Zr_{0.33}O_2$ prepared by traditional impregnation, such as the increased oxygen mobility in ceria–zirconia solid solutions and the improved stability of metallic state of platinum at high-temperature.

The air–fuel ratio ($\lambda$) always fluctuates when car accelerates or decelerates in actual working conditions. Thus, a lot of researches have been focused on the influence of the reductive/oxidative pre-treatments at certain temperatures on the properties of the catalysts by affecting the redox couple $Ce^{4+}/Ce^{3+}$, which plays a key role in the conversion of HC, CO and $NO_x$ [13–14]. Kozlov et al. [15] found that the redox treatment at 900 °C enhanced the reducibility of $Ce^{4+}$ in the $Al_2O_3$-supported $Ce_{0.45}Zr_{0.55}O_2$ sample with the appearance of a new low-temperature reduction feature at 320 °C. The features of the strong metal–support interaction (SMSI) have been summarized in the literatures [16–19]. Holmgren et al. [20] observed that a reduction in hydrogen at 200 or 300 °C resulted in a higher activity than reduction at 500 °C for a moderate-dispersed $Pt/CeO_2$ catalyst, but the choice of reduction temperature had no great influence on the activity for low-dispersed $Pt/CeO_2$. Fan et al. [14] reported that the oxidative/reductive alternate treatments affected the structure and performance of the $Pt/Ce_{0.67}Zr_{0.33}O_2$ catalyst by the SMSI. It was suggested that during the reductive treatment migration of $Ce^{4+}$ from the bulk to the surface of the

* Corresponding author. Tel.: +86 10 62772726; fax: +86 10 62772726.
*E-mail address:* duanweng@tsinghua.edu.cn (D. Weng).

0920-5861/$ – see front matter © 2010 Elsevier B.V. All rights reserved.
doi:10.1016/j.cattod.2010.02.013

support took place, while the diffusion process was reversed when the atmosphere was switched to an oxidative one.

In this work, Pd-doped $CeO_2$ catalyst was synthesized by sol–gel method in an attempt to maximize the metal–support interaction. The $H_2$–$O_2$ redox treatments at different temperatures were used to explore the structure reorganization on the catalytic activity under different treatment conditions. To this end, the catalysts were characterized by XRD, BET, Raman, CO-TPR, OSC and CO oxidation measurements.

## 2. Experimental

### 2.1. Catalyst preparation

Fresh Pd-doped $CeO_2$ catalyst was prepared by the citric-aided sol–gel method. The nitrates $Ce(NO_3)_3{\cdot}6H_2O$ and $Pd(NO_3)_2{\cdot}5H_2O$ were used as precursors. The nitrate solutions were carefully mixed according to the molar percentage of Pd of 1%. The citric acid was added as the complexing agent with a 1.2:1 ratio of the acid to metal ions including $Ce^{3+}$ and $Pd^{2+}$. Appropriate glycol was followed with the weight of 10% citric acid added. The blended solution was sufficiently mixed in a magnetic stirrer and heated at 100 °C until a spongy yellow gel was obtained. After being dried at 110 °C for 12 h, the gel was submitted to decomposition at 300 °C for 1 h and calcination at 500 °C for 3 h under a static air in a muffle. The powders were cooled to room temperature (RT) in the furnace.

For the redox treatments, the as-received powders were treated in a quartz tube by passing alternating gases at 300, 500 and 800 °C for 5 h, respectively, and the obtained powders were denoted as 300 redox, 500 redox, 800 redox. The alternating order of the gas mixtures was $H_2$ (2.8% in $N_2$, 200 ml/min, 10 s)–He (60 ml/min, 20 s)–$O_2$ (1.6% in $N_2$, 250 ml/min, 10 s)–He (60 ml/min, 20 s).

### 2.2. Catalyst characterizations

The X-ray diffraction analysis (XRD) was conducted on a Japan Science D/max-RB diffractometer employing Cu Kα radiation ($\lambda$ = 1.5418 Å). The X-ray tube was operated at 45 kV and 150 mA. The X-ray powder diffractograms were recorded at 0.02° intervals in the range $20^\circ \leq 2\theta \leq 80^\circ$ with 2 s count accumulation per step. The crystal phase was identified with the help of the JCPDS cards. The calculations and analyses based on the XRD data were assisted by the THX application software and the peak fitting was acquired according to a pseudo-Voigt profile function. The lattice parameters were calculated with the application of least-squares refinement of cell dimensions from powder data by Cohen's method. The average crystallite size of the mixed oxides was estimated according to Debye–Scherrer equation. The data for step-scanning XRD were recorded at 0.01° intervals in the range $39.0^\circ \leq 2\theta \leq 43^\circ$ with 3 s count accumulation per step.

The specific surface area was determined by Brunauer–Emmett–Teller (BET) method with an F-sorb 3400 instrument using He as carrier and $N_2$ as adsorbent.

The Raman spectra were acquired with a Renishaw RM 2000 microscopic confocal Raman spectrometer. The emission line at 632.8 nm from a He–Ne laser was focused on the samples (with an analyzing spot diameter of 5 mm) under microscope. The power of the incident beam on samples was 4.7 mW and the scattered radiation was collected at 1808 with the resolution of 1 $cm^{-1}$.

The temperature-programmed reduction (TPR) was performed in a microreactor. Before each measurement, 50 mg sample was treated in 2%$O_2$/He (100 ml/min) at 500 °C for 1 h followed by cooling down to RT in He. A flow of 4% CO/He (50 ml/min) was then introduced as reducing agent and the sample was heated up to 900 °C at a rate of 10 °C/min. The signals of CO uptake and $CO_2$ production as well as the $H_2$ production were collected by an on-line quadrupole mass spectrometer (Omnistar 200).

### 2.3. Oxygen storage capacity measurement

The oxygen storage capacity (OSC) measurement was conducted based on the method proposed by Yao and Yu Yao [21]. The measurement was carried out in a flow reactor system, designed for powder samples and equipped with solenoid valves for rapid introduction of 4% CO/(1% Ar + He) and 2% $O_2$/(1% Ar + He) pulses. Typically, 25 mg powders were loaded into a 1.0 cm i.d. quartz tube reactor and a total gas flow rate of 300 ml/min was employed. The signals of the outlet gas were detected by an on-line quadrupole mass spectrometer (Omnistar 200).

Two forms of OSC measurements, including successive CO pulse and dynamic CO–$O_2$ cycle, were applied to measure OSCC and DOSC, respectively. Before the successive CO pulse measurement test, all samples were pre-oxidized in 2% $O_2$/He at 300 °C for 20 min and flushed by He for 30 min at 500 °C. The test procedure consisted of the cycles of 5-s-long CO/(Ar + He) injection and 40-s-long outgassing of pure He on the samples at that temperature. The OSCC was quantified by integrating the concentration of $CO_2$ produced in the first ten CO/(Ar + He) pulses. In the dynamic CO–$O_2$ mode, OSC measurement was operated at certain temperatures by alternately injecting CO/(Ar + He) and $O_2$/(Ar + He) on the samples with duration of 5 s for each gas, which meant a test frequency of 0.1 Hz. DOSC was quantified in terms of micromole of $CO_2$ per gram of catalyst ($\mu$mol $CO_2/g_{cat}$) by integrating the concentration of $CO_2$ produced during every single CO–$O_2$ cycle.

To further investigate the oxygen release behavior of the samples, a static CO step measurement was conducted at temperatures ranging from 350 to 550 °C. At the beginning of this measurement, a 20-min-long oxidation by $O_2$ was introduced to the samples. We assumed that the ceria species in the materials entirely existed in the form of $Ce^{4+}$ after this pretreatment. After the oxidation, the samples were purged in pure He for 30 min to remove oxygen from the reactor system and then were exposed to the CO/(Ar + He) flow of 300 ml/min for 2 min. The signals of the outlet gas were also collected by the on-line quadrupole mass spectrometer.

### 2.4. Activity measurement

50 mg catalyst was mixed with coarse quartz particles to make the total volume of the mixture reach 0.5 ml. The mixture was loaded in a quartz reaction tube with the diameter of 10 mm. The carbon monoxide oxidation activity was evaluated by passing a gas mixture of 2%CO, 1%$O_2$ and He in balance. The reactor was heated from RT to 400 °C in the flow stream at a gas space velocity (GSV) of 60 000 $h^{-1}$. The concentrations of $O_2$, CO and $CO_2$ were detected by the on-line quadrupole mass spectrometer.

## 3. Results and discussion

### 3.1. CO oxidation activity

In order to investigate the influence of redox treatments at different temperatures on the catalytic activity of the Pd-doped $CeO_2$ catalyst, the CO oxidation tests were performed and the obtained light-off curves are shown in Fig. 1. The fresh sample exhibits an excellent activity with the onset temperature is below 100 °C and complete conversion temperature is at 200 °C. It is interesting that the 300 redox sample behaves a even better activity compared with the fresh one, which shows a similar light-off curve with a shift to lower temperature by 20 °C. With the further increase of the redox temperature, the activity of the treated samples decreases again. The 800 redox sample is severely deactivated for CO oxidation with

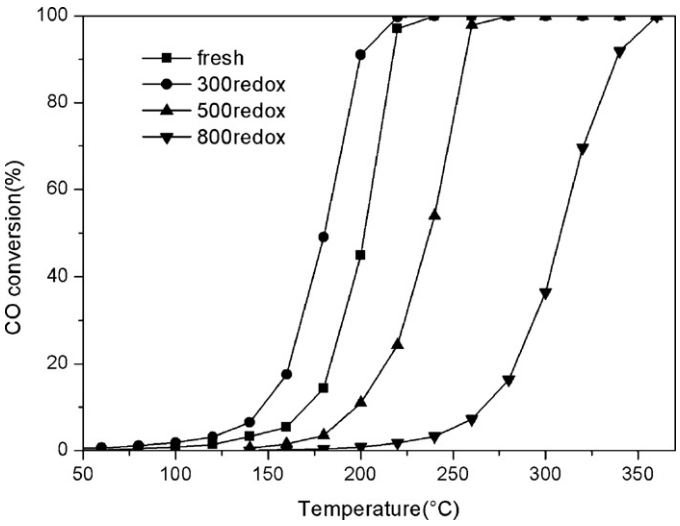


**Fig. 1.** Light-off curves of CO oxidation over the catalysts. Reaction conditions: 2%CO/1%$O_2$/$N_2$, 500 ml/min.

the onset temperature at 187 °C and complete conversion at 350 °C. These variations of the activity are suggested to be related to the structure reorganization of the catalyst during the redox treatment.

### 3.2. OSC properties

#### 3.2.1. OSCC

The OSC values at each CO pulse and OSCC values accumulated at 200 and 400 °C are shown in Fig. 2a and b, respectively. The amount of the most readily available oxygen ("fast" OSC) from the catalyst was quantified according to the oxygen consumed in the first CO pulse, and the oxygen participating in the reactions from the second to the tenth pulse was considered to be released from the bulk of particles [22]. The OSCC values follow the sequence of 300 redox > fresh > 500 redox > 800 redox at both 200 and 400 °C. The releasable oxygen from PdO can be estimated according to the nominal content of Pd in the catalyst by assuming all the Pd species in the form of PdO. The estimated value is 58 μmol/$g_{cat}$, which is much larger than those obtained in the first CO pulse. Thus, it can be considered that the most readily available oxygen at 200 °C comes from the surface PdO species and Pd-Ce interface may be also involved. The reaction rate depends on adsorption of CO and its reaction with active oxygen, thus the amount of available Pd active sites per gram of catalyst is the determining factor in this case. The 300 redox sample exhibits the highest fast OSC, which may be related to the surface reconstruction probably including the leaching of Pd from the ceria lattice and formation of small Pd crystallites and Pd-Ce interface exposed on the surface of the catalyst.

In the case of OSC tests at 400 °C (Fig. 2b), the amount of readily available oxygen is much larger than that in PdO, so the $CeO_2$ support also plays an important role. At this temperature, the promoting effect of Pd on the total OSC does not seem to be so obvious as at 200 °C since the OSC of the $CeO_2$ based support itself is quite high [23,24]. It is noticed that the total OSC of the fresh sample is close to that of the 500 redox one at 200 °C, while it is close to that of the 300 redox sample at 400 °C. This phenomenon can be explained via the SMSI effect at different reaction temperatures. Pd mainly provides active sites for CO adsorption, and CO reaction is not the control process. The diffusion of $O^{2-}$ driven by the oxygen concentration gradient from the bulk to the surface determines the OSC behavior of the catalyst at high-temperature [25].

It should be also noticed in Fig. 2 that the OSC values at 3rd–10th CO pulses for 500 redox sample are higher than those for 800 redox

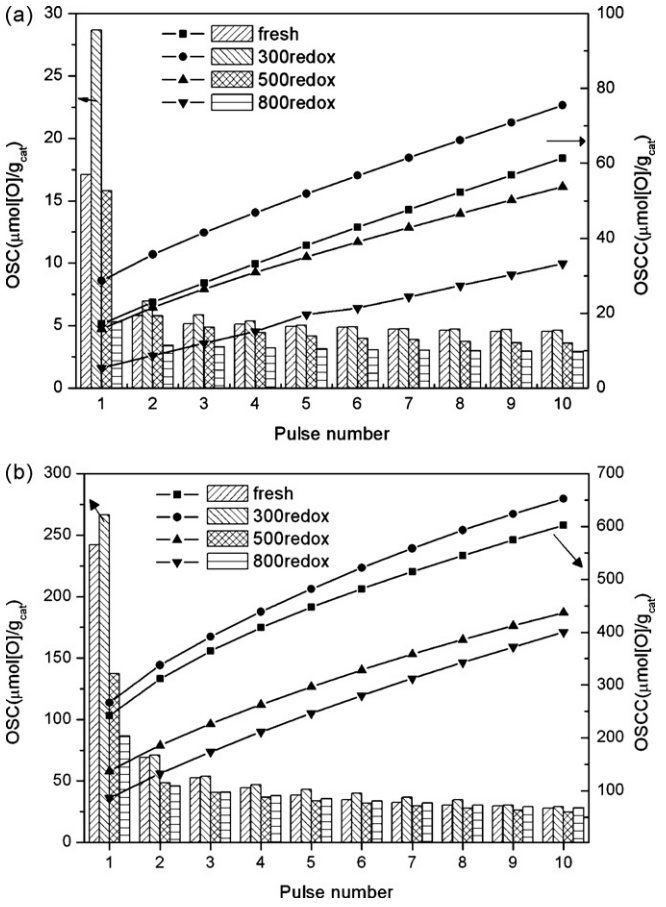


**Fig. 2.** OSC at each CO pulse and accumulated OSCC values at (a) 200 and (b) 400 °C.

sample at 200 °C, while the order is reversed at 400 °C. This phenomenon should be related to the lattice reconstruction of the catalyst caused by the redox treatment. The encapsulation of Pd species by the support at high-temperature (800 °C) facilitates the mobility of bulk oxygen in ceria to some extent [26].

#### 3.2.2. DOSC

Dynamic OSC can reflect the oxygen storage/release capacity during the quick alternating atmosphere under actual conditions. The DOSC values of the catalysts at different temperatures are shown in Fig. 3. Agreeing well with the OSCC results, DOSC values follow the same sequence of 300 redox > fresh > 500 redox > 800 redox over the whole testing temperature range. Again, it is noticed that the dynamic OSC of the fresh sample is close to that of the 500 redox one at 200 °C, while it is close to that of the 300 redox sample at 400 and 500 °C. Since the DOSC measurement process involves the activation and reaction of gaseous oxygen, the DOSC data are much higher than the OSC values obtained at 1st CO pulse in the OSCC experiment. In this case, the mobility of bulk oxygen is no longer the controlling factor, and the availability of active Pd sites becomes predominant. Thus, the DOSC values of the 500 redox sample are always higher than those of the 800 redox sample due to the exposure of more Pd active sites.

#### 3.2.3. CO step measurement

The $CO_2$ concentration during the CO step measurement was monitored as a function of time. The instantaneous rates for $CO_2$ production at certain $Ce^{3+}$/Ce ratios, denoted as $R_{CO_2}$, were calculated based on the analyzing method well established by Hori et al. [27]. As shown in Fig. 4, the reduction ratio of the material at the time of interest, $t_i$, was determined by integrating the $CO_2$

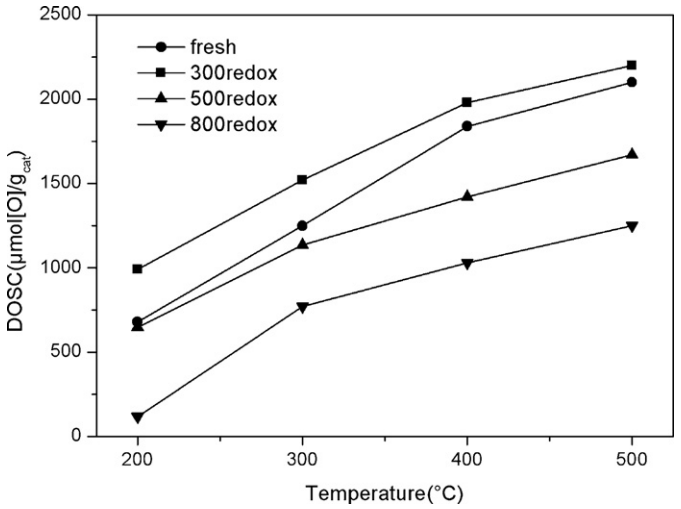


**Fig. 3.** Dynamic OSC values obtained from the production of $CO_2$ at different temperatures.

formed from the start of the pulse, $t_0$, to $t_i$ (e.g., $t_1$ and $t_2$). Then, the integrated $CO_2$ formed was mass balanced with the O atoms that released from the sample to determine the reduction ratio.

The evolution of $R_{CO_2}$ as a function of temperature is given in Fig. 5 as Arrhenius coordinates and the activation energy ($E_a$) for CO oxidation was estimated according to the slope of the linear function. Different Arrhenius plots are obtained at $Ce^{3+}/Ce = 1.5\%$ (Fig. 5a) and 6% (Fig. 5b), indicating that $E_a$ are to some extent reduction-ratio dependent. Along with the increase of reduction ratio, the slopes of the linear functions for all the samples present a sharp increase. It suggests that the rate-limiting step for CO catalytic oxidation varies with the participating oxygen species originated from different parts of the particles. It can be seen that the rate-limiting processes of the catalysts are different at low reduction ratio of the support, and become similar when the reduction process penetrates into the bulk of the particles.

To examine the temperature point where the rate-limiting step alters, the $E_a$ values were estimated at the reduction ratios of 1.5%, 3%, 6% and 12%, respectively, and the results are shown in Fig. 6. At the initial stage of reaction ($Ce^{3+}/Ce = 1.5\%$), the extremely low $E_a$ for the 300 redox sample indicates that there are much more labile oxygen on the surface of this catalyst than the fresh and

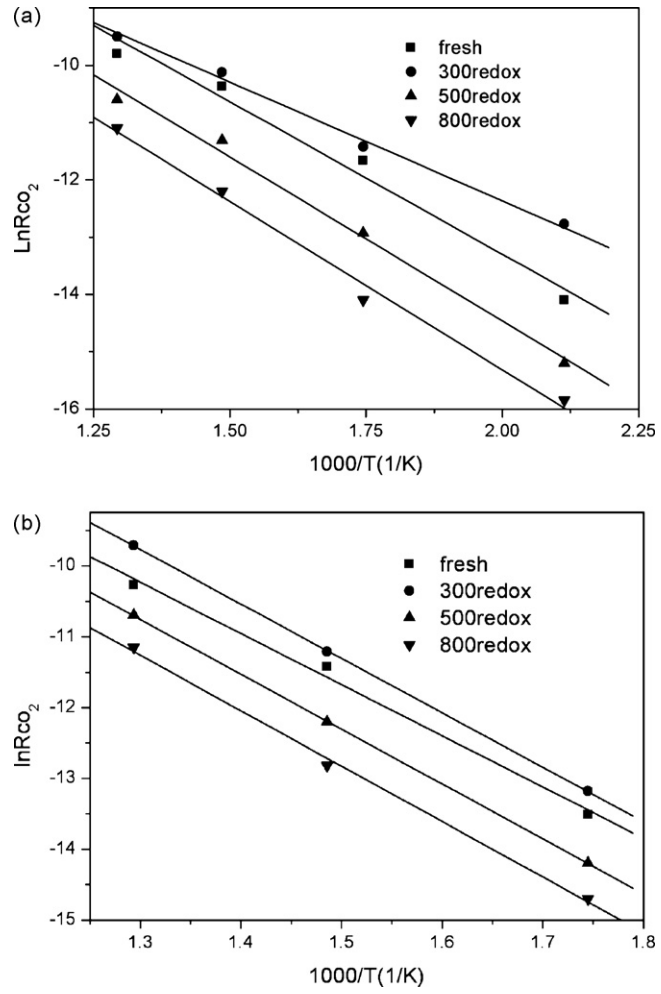


**Fig. 5.** Arrhenius plots for the samples when (a) $Ce^{3+}/Ce = 1.5\%$ and (b) $Ce^{3+}/Ce = 6\%$.

other treated samples. The amount of readily available surface oxygen follows the order of 300 redox > fresh > 500 redox > 800 redox. The $E_a$ increases with the increase of the reduction ratio for all the samples which means that the activation of oxygen becomes difficult. The fresh sample shows the lowest $E_a$ when the reduction

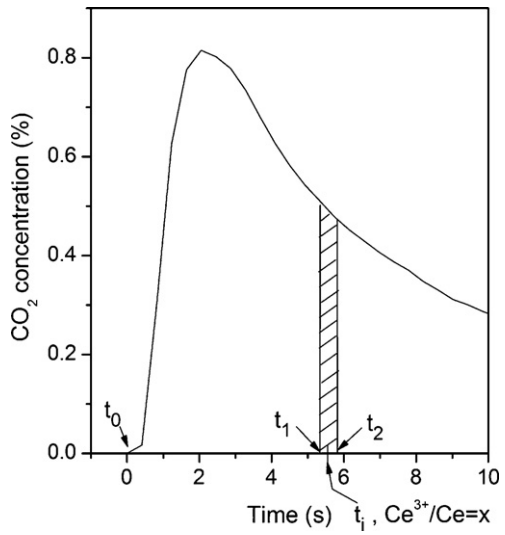


**Fig. 4.** Schematic representation of the calculation of reaction rates.

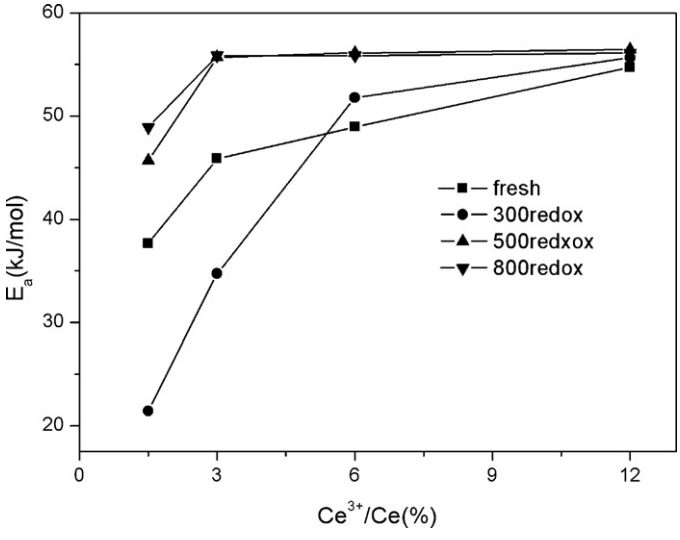


**Fig. 6.** Activation energies for CO oxidation at different reduction ratios of the support.

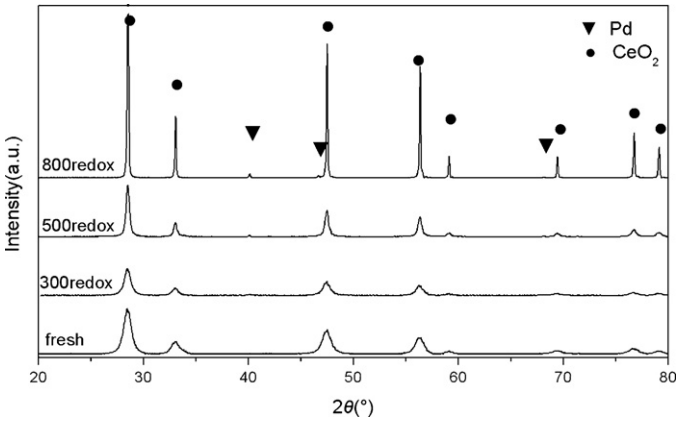


**Fig. 7.** XRD patterns of the fresh and treated Pd-doped $CeO_2$ samples.

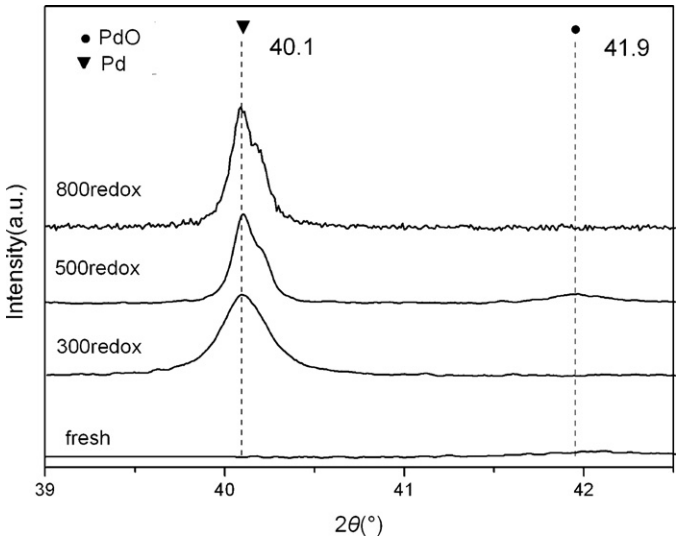


**Fig. 8.** Step-scanning XRD patterns of the fresh and treated Pd-doped $CeO_2$ samples.

ratio reaches 6%, which may be related to the doping of palladium in the $CeO_2$ lattice and the activation of lattice oxygen. When the oxygen diffusion process penetrates into the bulk of the oxide particles ($Ce^{3+}/Ce = 12\%$), the $E_a$ becomes similar to each other for all the samples. Again, it confirms that the oxygen storage and activation is related to the structure of the catalyst. The consumption of readily available oxygen takes place at ca. 3% reduction ratio for the 500 redox and 800 redox samples, while that occurs at ca. the 6% reduction ratio for the fresh and especially 300 redox samples.

### 3.3. Structural and textural properties

The importance of the surface structure of the catalyst is highlighted according to the above activity results. In order to study the structure changes during the redox treatments at different temperatures, the XRD, Raman and TPR experiments were carried out. The X-ray diffraction patterns of the fresh and treated Pd-doped $CeO_2$ samples are shown in Fig. 7. The main peaks are consistent with the characteristic peaks of cubic $CeO_2$ for all the samples. The sharpening of the characteristic peaks for the redox treated samples implies a sintering of the support during the treatments especially for the 500 redox and 800 redox samples. It can be seen from Table 1 that the mean crystallite size of ceria increases and correspondingly the BET surface area of the catalysts decreases with ramping the redox treatment temperature.

The mean lattice constant of ceria was calculated according to the method of Kimura [28]. The (Pauling) ionic radii taken for calculation are 0.086 and 0.097 nm for $Pd^{2+}$ and $Ce^{4+}$, respectively. Both PdO and $CeO_2$ belong to the cubic structure. The lattice constant of $CeO_2$ prepared by the same sol–gel method is 0.5426 nm, which is larger than that of the fresh Pd-$CeO_2$ sample (0.5417 nm). Thus, it is speculated that the Pd cations with smaller ionic radius are at least partially doped into ceria, resulting in shrinkage of the ceria crystal lattice. The lattice constant of ceria in the 300 redox sample is the same as that of the fresh one. Combined with the similar surface area, it can be concluded that the redox treatment at 300 °C has little influence on the bulk structure of the catalyst. On the other hand, the lattice constant of the sample decreases with the redox treatment at higher temperatures (500 and 800 °C). Some diffraction peaks of the Pd phase are observed for the treated samples, which increase in intensity with the ramping the treatment temperatures.

**Table 1**
Structural and textural properties of the fresh and treated samples.

| Sample | Lattice constant of ceria (nm) | Crystallite size of ceria (nm) | $S_{BET}$ ($m^2/g$) |
|---|---|---|---|
| Fresh | 0.5417 | 8.6 ± 0.1 | 29.9 |
| 300 redox | 0.5417 | 10.4 ± 0.2 | 30.5 |
| 500 redox | 0.5414 | 22.3 ± 0.4 | 8.4 |
| 800 redox | 0.5411 | 68.9 ± 1.2 | 3.8 |

In order to observe the status of Pd species more clearly, the step-scanning XRD measurements were carried out and the results are shown in Fig. 8. Only a broad and weak PdO (1 1 0) peak centered at 41.9° is observed for the fresh sample, implying that Pd species are finely dispersed on the surface of $CeO_2$ or even dissolved into the $CeO_2$ lattice. Another distinct peak centered at 40.1° arises from the diffraction on (1 1 1) plane of metallic Pd occurs for the treated samples, which strongly supports the formation and aggregation of Pd crystallites during the redox treatment. The intensities of these peaks are similar to each other for the treated samples. The metallic Pd may be related to the sintering of the surface Pd on the 300 redox sample species since its bulk structure changes little, while the occurrence of the Pd phase may arise from both the sinter of surface Pd species and exudation of Pd from the support lattice. There are no PdO peaks observed for the 300 redox and 800 redox samples, while a broad PdO (1 1 0) peak centered at 41.9° is observed on the 500 redox sample. This may be related to the oxidation of the surface Pd species to PdO.

Since the X-ray pattern reflects the cation order–disorder and lattice distortion, and is poorly sensitive to oxygen sublattice, the nuances in the short-range oxygen displacement of the solid solutions were examined by Raman spectroscopy, which is sensitive to both M–O bond arrangement and lattice defects [29]. As shown in Fig. 9a, a prominent peak at 461 $cm^{-1}$, owning to $F_{2g}$ Raman active mode of the fluorite-like structure, is observed for all the samples. The leaching of palladium during the redox treatments at 300 and 500 °C may cause a decrease of lattice homogeneity, while the encapsulation of palladium by the support after the high-temperature redox treatment causes a reverse result [15]. The shift of the $F_{2g}$ peak from 460 $cm^{-1}$ for the 300 redox sample to 464 $cm^{-1}$ for the 800 redox sample may be another evidence for the reconstruction of the ceria lattice. The $F_{2g}$ peak for pure ceria is 465 $cm^{-1}$. The blue shifts for the treated samples may be related to the insertion of Pd into the lattice. As shown in Fig. 9b, the presence of a band at ca. 650 $cm^{-1}$ for the 500 redox sample is ascribable to the $B_{2g}$ Raman mode of PdO [30], which again confirms the formation of bulk PdO particles on the surface of the catalyst and is consistent with the step-scanning XRD results.

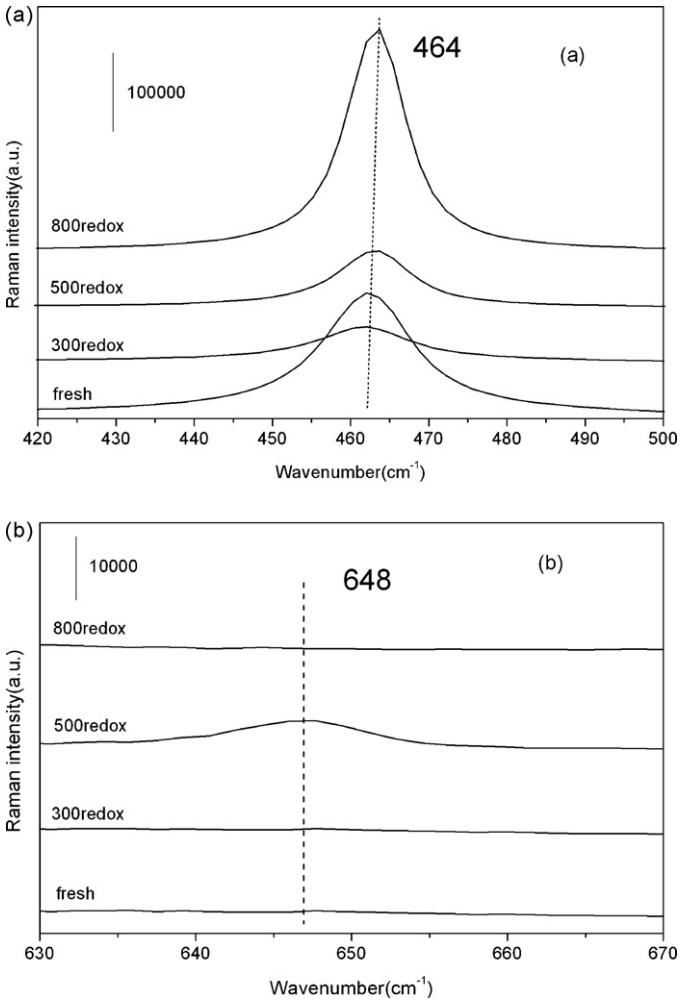


**Fig. 9.** Raman spectra of the (a) fresh and (b) treated Pd-doped $CeO_2$ samples.

### 3.4. Redox property

The CO-TPR profiles of the samples are shown in Fig. 10. The first peak of the fresh, 300 redox, 500 redox and 800 redox samples is located at 124, 130, 155 and 190 °C, respectively, which is attributed to reduction of dispersed PdO. [31]. Pd ions are considered to be incorporated into the ceria lattice or finely dispersed PdO

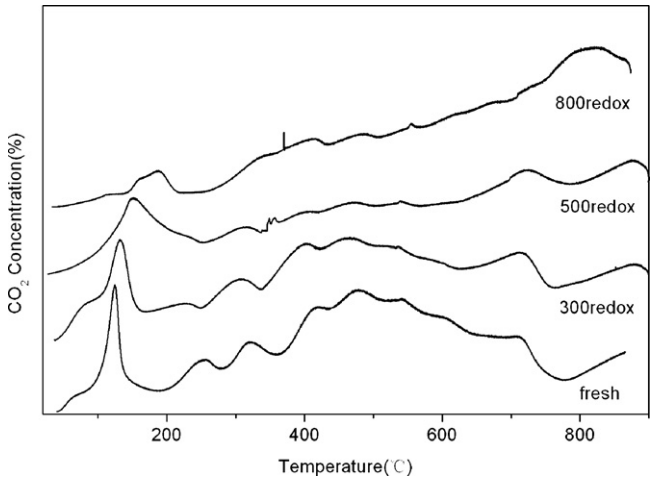


**Fig. 10.** CO-TPR profiles of the fresh, redox and aged Pd/$CeO_2$ samples.

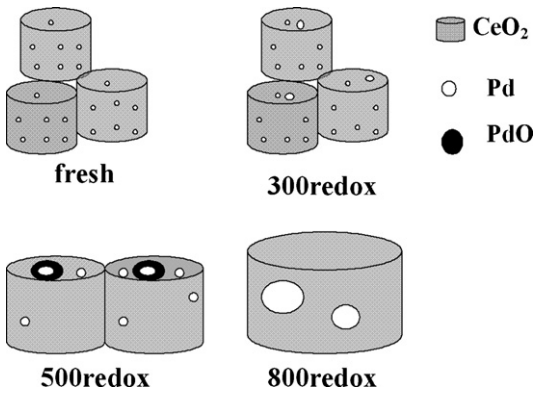


**Fig. 11.** Schematic of the microstructural features of Pd-$CeO_2$ after the redox treatments at different temperatures.

on the surface of ceria crystallites for the fresh samples. The peaks around 400 and 700 °C for the fresh, 300 redox and 500 redox samples are attributed to the reduction of the $CeO_2$ on surface and in bulk facilitated by Pd, respectively. This strong interaction between metal and support experience a great loss due to the sintering of Pd crystallites for the 800 redox sample. As a result, the reduction peak of $CeO_2$ in bulk shifts to the temperature as high as 830 °C, the reduction temperature is almost the same as the ceria. These phenomena are consistent with the XRD results. The doping of Pd in the fresh sample lowers the reduction temperature of cubic $CeO_2$ to about 700 °C. Since the 300 redox treatment mainly affects the surface properties of the catalysts, its reduction profile is similar to that of the fresh sample. It should be demonstrated that the low-temperature reduction peak related to the surface Pd species is prolonged to even lower temperature, implying a stronger redox property in respect to .the fresh sample.

There is $CO_2$ formed even below 100 °C for the fresh sample, which is related to the Pd-Ce interface according to the results of Fernandez-García [32]. Thus, the increase of this low-temperature peak for the 300 redox sample can be ascribed to the enlarged of the Pd-Ce interface due to the leaching of subsurface Pd species. The PdO peak of the 500 redox sample is the largest among the samples due to the migration of Pd from the $CeO_2$ support. The smallest PdO peak of the 800 redox sample is ascribed to the encapsulation of palladium oxide by the $CeO_2$ support after the redox treatment at high-temperature.

## 4. Discussion

The redox treatments at different temperatures result in various effects on the surface and bulk structure of Pd-$CeO_2$ catalyst. A schematic of microstructure of different samples is depicted in Fig. 11. Based on this structure model, the CO oxidation activity and the oxygen storage capacity of the Pd-$CeO_2$ catalyst can be generally interpreted.

It is generally accepted that CO oxidation on the supported noble metal catalysts proceeds via the LH surface reaction between the adsorbed CO and activated oxygen [33]. CO oxidation is a structure insensitive reaction, and on PM/$CeO_2$ this reaction is supported to proceed according to a bi-functional pathway involving CO adsorbed on the metal and oxygen from ceria at the metal-ceria interface [34,35]. So both the Pd-Ce interface and active Pd sites play important roles in CO oxidation. At a low-temperature such as 300 °C, the redox treatment basically affects the surface features of the catalyst. It causes the short-range migration of palladium species from the subsurface region onto the surface of the catalysts and thus creates more available Pd-Ce interface sites. As a result, this sample shows the highest activity. The treatments at

higher temperatures result in the exudation of Pd out of the ceria lattice. The leached Pd/PdO crystallites aggregate on the surface of the catalyst and form bulk Pd/PdO particles at 500 °C. Thus, the amount of available Pd-Ce interface sites decreases and the catalyst experiences a severe loss of activity. The formed PdO particles are encapsulated again due to the collapse of pore structure of the support after the redox treatment at a temperature as high as 800 °C. In this way, the amount of available Pd active sites sharply decreases accompanied with the severe deactivation of the catalyst.

## 5. Conclusion

In this study, a Pd-doped $CeO_2$ catalyst was synthesized by sol–gel method and treated in a $H_2/O_2$ redox atmosphere at 300, 500 and 800 °C, respectively. The redox treatments at different temperatures have different impacts on the structure and redox properties of Pd-$CeO_2$ system: the low-temperature treatment mainly affects the surface Pd species, while the high-temperature treatment affects both the bulk Pd and $CeO_2$ with a strong synergetic effect between metal and support. The sample treated at 300 °C performs the highest CO oxidation activity and lowest oxygen activation energy, which is related to the enlarged Pd-Ce interface.

## Acknowledgments

The authors would like to acknowledge the Ministry of Science and Technology, PR China for the financial support of Project 2009AA064803 and National Natural Science Foundation of China for the financial support of Project 50972069. Moreover, we would also thank the Center of Analysis and State Key Laboratory of New Ceramics & Fine Process in Tsinghua University.

## References

[1] Y.C. Ma, Q.J. Ge, W.Z. Li, H.Y. Xu, J. Nat. Gas Chem. 17 (2008) 387.
[2] P.Y. Sheng, W.W. Chiu, A. Yee, S.J. Morrison, H. Idriss, Catal. Today 129 (2007) 313.
[3] Shinichi Matsumoto, Catal. Today 90 (2004) 183.
[4] Y. Guo, G.Z. Lu, Z.G. Zhang, S.H. Zhang, Y. Qi, Y. Liu, Catal. Today 126 (2007) 296.
[5] A. Martínez-Arias, M. Fernández-García, A.B. Hungría, A. Iglesias-Juez, J.A. Anderson, Catal. Today 126 (2007) 90.
[6] M.S. Hedge, Giridhar Madras, Accoumts Chem. Res. 42 (2009) 704.
[7] Parthasarathi Bera, K.C. Patil, Y.V. Jayaram, G.N. Subbanna, M.S. Hegde, J. Catal. 196 (2000) 293.
[8] Sounak Roy, A. Marimuthu, M.S. Hegde, Giridhar Madras, Appl. Catal. B 71 (2007) 23.
[9] K.R. Priolkar, Parthasarathi Bera, P.R. Sarode, M.S. Hegde, S. Emura, R. Kumashiro, N.P. Lalla, Chem. Mater. 14 (2002) 2120.
[10] Gargi Dutta, Umesh V. Waghmare, Tinku Baidya, M.S. Hegde, K.R. Priolkar, P.R. Sarode, Chem. Mater. 18 (2006) 3249.
[11] N. Barrabe, K. Fottinger, A. Dafinov, F. Medina, G. Rupprechter, J. Llorca, Appl. Catal. B 87 (2009) 64.
[12] X.D. Wu, J. Fan, R. Ran, D. Weng, Chem. Eng. J. 109 (2005) 133.
[13] L.F. Liotta, A. Longo, A. Macaluso, A. Martorana, G. Pantaleo, A.M. Venezia, Appl. Catal. B 48 (2004) 133.
[14] J. Fan, X.D. Wu, R. Ran, D. Weng, Appl. Surf. Sci. 245 (2005) 162.
[15] Alexander I. Kozlov, Do Heui Kim, Aleksey Yezerets, Paul Andersen, Harold H. Kung, Mayfair C. Kung, J. Catal. 209 (2002) 417.
[16] Y.W. Zhang, J.H. Zhou, Z.H. Wang, J.Z. Liu, K.F. Cen, Int. J. Hyderogen Energy 33 (2008) 2211.
[17] A. Mohamed, B. Valerie, T. Raymonde, Appl. Catal. A 297 (2006) 48.
[18] C. Bozo, N. Guilhaume, J.M. Herrmann, J. Catal. 203 (2001) 393–406.
[19] S. Bernal, J.J. Calvino, M.A. Cauqui, J.M. Gatica, C. Larese, J.A.P. Omil, Catal. Today 50 (1999) 175.
[20] A. Holmgren, F. Azarnoush, E. Fridell, Appl. Catal. B 22 (1999) 49.
[21] H.C. Yao, Y.F. Yu Yao, J. Catal 86 (1984) 254.
[22] J. Fan, D. Weng, X.D. Wu, X.D. Wu, R. Ran, J. Catal. 258 (2008) 177.
[23] B. Sumeya, D. Claude, D. Daniel, Catal. Today 73 (2002) 233.
[25] P. Fornasiero, J. Kaspar, M. Graziani, Appl. Catal. B 22 (1999) 11.
[26] H. Vidal, J. Kašpar, M. Pijolat, G. Colon, S. Bernal, A. Cordón, V. Perrichon, F. Fally, Appl. Catal. B 30 (2001) 75.
[24] M.W. Zhao, M.Q. Shen, J. Wang, J. Catal. 248 (2007) 258.
[27] C.E. Hori, Brennera, K.Y.S. Ng, K.M. Rahmoeller, D. Belton, Catal. Today 50 (1999) 299.
[28] M. Ozawa, M. Kimura, A. Isogai, J. Alloys Compd. 193 (1993) 73.
[29] S. Damyanova, B. Pawelec, K. Arishtirova, M.V. Martinez Huerta, J.L.G. Fierro, Appl. Catal. A 337 (2008) 86.
[30] A. Iglesias-Juez, A. Martínez-Arias, M. Fernández-García, J. Catal. 221 (2004) 148.
[31] A. Talo, J. Lahtinen, P. Hautojärvi, Appl. Catal. B 5 (1995) 221.
[32] M. Fernández-García, A. Martínez-Arias, L.N. Salamanca, J.M. Coronado, J.A. Anderson, J.C. Conesa, J. Soria, J. Catal. 187 (1999) 474.
[33] T. Engel, G. Ertl, Adv. Catal. 28 (1979) 1.
[34] H.Q. Zhu, Z.F. Qin, W.J. Shan, W.J. Shen, J.G. Wang, J. Catal. 233 (2005) 41.
[35] R. Rajasree, J.H.B.J. Hoebink, J.C. Schouten, J. Catal. 223 (2004) 36.